

On the collision of laminar jets: fluid chains and fishbones

By JOHN W. M. BUSH AND ALEXANDER E. HASHA

Department of Mathematics, Massachusetts Institute of Technology,
77 Massachusetts Avenue, Cambridge, MA 02139, USA

(Received 5 December 2002 and in revised form 20 March 2004)

We present the results of a combined experimental and theoretical investigation of the family of free-surface flows generated by obliquely colliding laminar jets. We present a parameter study of the flow, and describe the rich variety of forms observed. When the jet Reynolds number is sufficiently high, the jet collision generates a thin fluid sheet that evolves under the combined influence of surface tension and fluid inertia. The resulting flow may take the form of a fluid chain: a succession of mutually orthogonal links, each composed of a thin oval film bound by relatively thick fluid rims. The dependence of the form of the fluid chains on the governing parameters is examined experimentally. An accompanying theoretical model describing the form of a fluid sheet bound by stable rims is found to yield good agreement with the observed chain shapes. In another parameter regime, the fluid chain structure becomes unstable, giving rise to a striking new flow structure resembling fluid fishbones. The fishbones are demonstrated to be the result of a Rayleigh–Plateau instability of the sheet's bounding rims being amplified by the centripetal force associated with the flow along the curved rims.

1. Introduction

The collision of laminar jets is one of the generic source geometries for the generation of fluid sheets (Dombrowski & Fraser 1954), the dynamics and stability of which have received a great deal of attention owing to their relevance in spray atomization (Bayvel & Orzechowski 1993; Lefebvre 1989). We here present the results of an experimental investigation of the collision of high-Reynolds-number laminar jets. We explore a broad parameter range and observe a rich variety of flow structures, from the single oscillating jet that obtains at low flow rates, to the violent disintegration of flapping sheets at high flow rates. We focus our attention on two previously unexplored flow structures that arise at intermediate flow rates: chains and fishbones.

Figure 1 illustrates a fluid chain, a steady flow structure composed of thin fluid sheets bound by relatively thick cylindrical rims generated by the oblique collision of equal laminar fluid jets. Individual links in the chain are mutually orthogonal (figure 2), and decrease successively in size until the chain coalesces into a cylindrical stream. Fluid chains may be produced in a variety of physical settings; for example, when wine is poured from a lipped jug, when rivulets of water flow off a leaf or sharp ledge, and during micturition. Fluid chains have been reported elsewhere (Rayleigh 1879 and references therein; Dombrowski & Fraser 1954; Johnson *et al.* 1996); however, a quantitative study of their form has not been undertaken. They were first

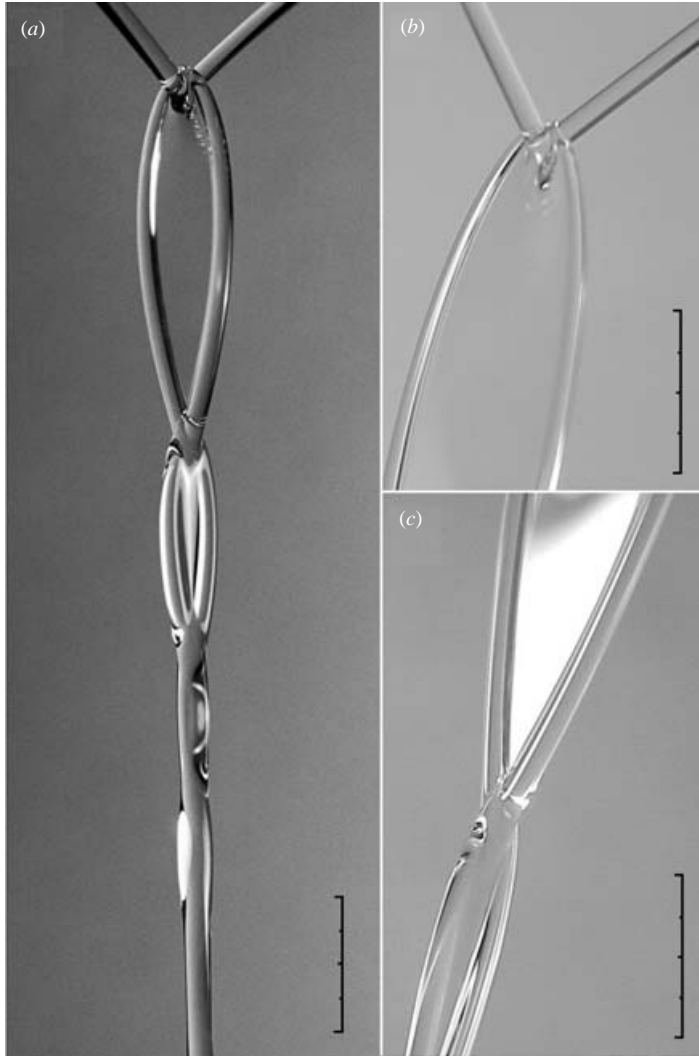


FIGURE 1. (a) A fluid chain resulting from the collision of a pair of identical laminar jets of a glycerol–water solution: $\nu = 20 \text{ cS}$, $R_j = 0.08 \text{ cm}$, $Q = 9.0 \text{ cm}^3 \text{ s}^{-1}$, $\sigma = 66 \text{ dyn cm}^{-1}$, $\rho = 1.19 \text{ g cm}^{-3}$. (b) A close-up of the collision that produces a thin flat sheet of fluid in the plane orthogonal to the plane of the two jets. Liquid accumulates at the edges of the sheet to produce thick circular rims that are drawn inward by surface tension. (c) The juncture between links of a fluid chain. The thick circular rims collide, producing another thin sheet in the plane orthogonal to the first link. The process repeats until the oscillations are damped through viscous dissipation. Scale bars: 1 cm.

observed by the authors in an exploratory experimental study of viscous water bells (Buckingham & Bush 2001); in certain parameter regimes, fluid chains were found to emerge from the corners of the polygonal sheet, as is evident in figure 3.

When two identical high-Reynolds-number laminar fluid jets collide at sufficiently high speed that gravity is negligible, the subsequent dynamics is dominated by fluid inertia and surface tension. The collision generates a fluid sheet in a plane perpendicular to the plane of incidence of the jets. Within the sheet, fluid is shot radially away from the point of impact of the jets at roughly uniform speed. The

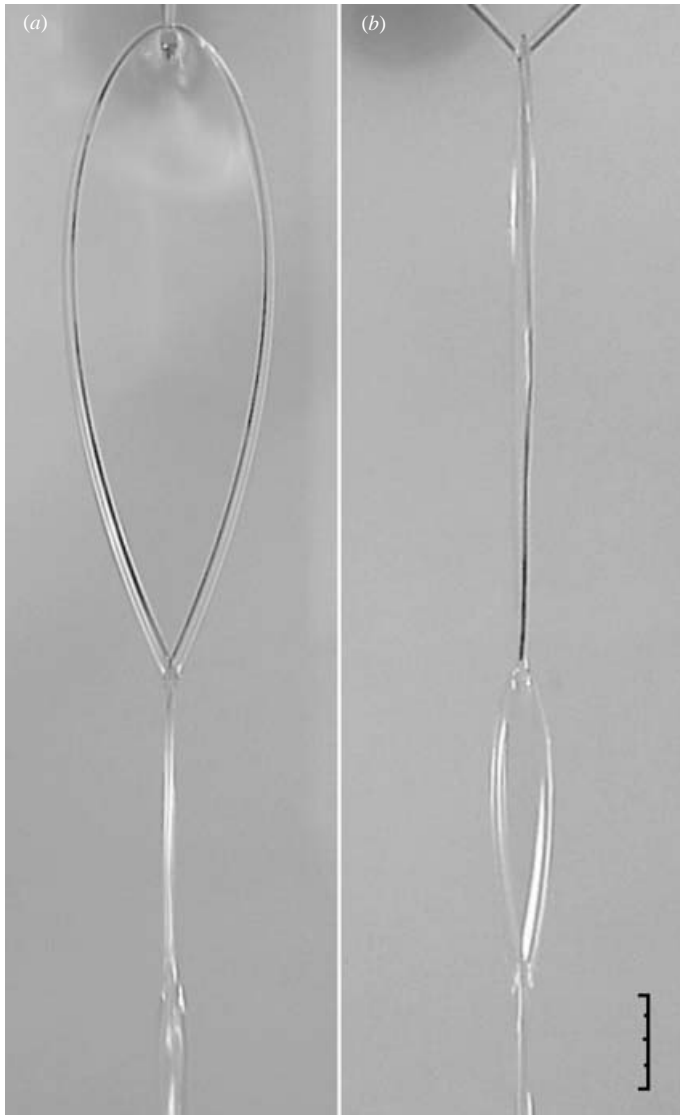


FIGURE 2. Front and side views of the fluid chain resulting from the collision of a pair of identical laminar jets. The first link, of length 6.3 cm, is evident in (a), the second in (b). Scale bar: 1 cm.

sheet thus thins as $1/r$, where r is the radial distance from the point of impact, until reaching the sheet's edge. The curvature force associated with the surface tension acts normal to the edges of the fluid sheet and so acts to limit its lateral extent. Moreover, the curvature force causes the sheet to retract and ultimately close, thus forming the apex of the first link. Fluid accumulates at the edges of the sheet to form relatively thick rims that bound the fluid sheet. When these rims collide at the apex of the link, they give rise to another thin sheet in the plane perpendicular to the first link. The process repeats, producing mutually orthogonal links that decrease progressively in size until the chain coalesces into a cylindrical stream through the action of viscosity (figure 1).



FIGURE 3. A polygonal fluid sheet (Buckingham & Bush 2001) generated by extruding a glycerine–water solution of viscosity 10 cS from a circular annulus of diameter 1 cm. Fluid chains are seen to emerge from the corners of the polygon. Scale bar: 1 cm.

Fluid chains may alternatively be understood as large-amplitude oscillations of a fluid jet with a non-circular cross-section. Rayleigh (1879) and Bohr (1909) examined the small-amplitude vibrations that arise when a laminar fluid jet is extruded from an elliptical orifice. As the jet leaves the orifice, surface tension causes it to seek out a circular cross-section; however, if the jet Reynolds number is sufficiently high, inertia causes an overshoot. Bohr (1909) demonstrated that the form of the resulting inertial–capillary oscillations may be used as a means to deduce surface tension. Fluid chains may be thought of as the large-amplitude limit of these inertial–capillary oscillations, in which the jet is composed of a thin film and relatively thick bounding rims.

Taylor (1960) considered the shape of sheets generated by the collision of laminar water jets. In his study, the sheet had unstable rims: once fluid reached the rim, it was immediately ejected in the form of droplets. Consequently, flow along the rims was not dynamically important, and Taylor deduced the sheet shape simply by equating the normal inertial force with the curvature force. In particular, the sheet radius was found to be well-described by the Taylor radius, $r_T(\theta) = \rho u_0 Q(\theta) / (2\sigma)$, where u_0 is the uniform sheet speed, $Q(\theta)$ is the flux distribution within the sheet (see figure 9) and ρ and σ denote the fluid density and interfacial tension. In our experimental study of fluid chains, the fluid viscosity is approximately 10–100 times that of water, and the sheet rims are stable. Consequently, the force balance governing the sheet shape is altered substantially, and we must consider explicitly the coupling between the rim and sheet dynamics. Specifically, flow along the rims results in a centripetal force that must appear in the normal force balance at the rim.

Fluid chains provide a relatively simple test geometry for a theoretical description of the dynamics of thin sheets bound by stable rims. In this paper, we build upon the theoretical work of Taylor (1959*b*) in developing a system of equations governing the

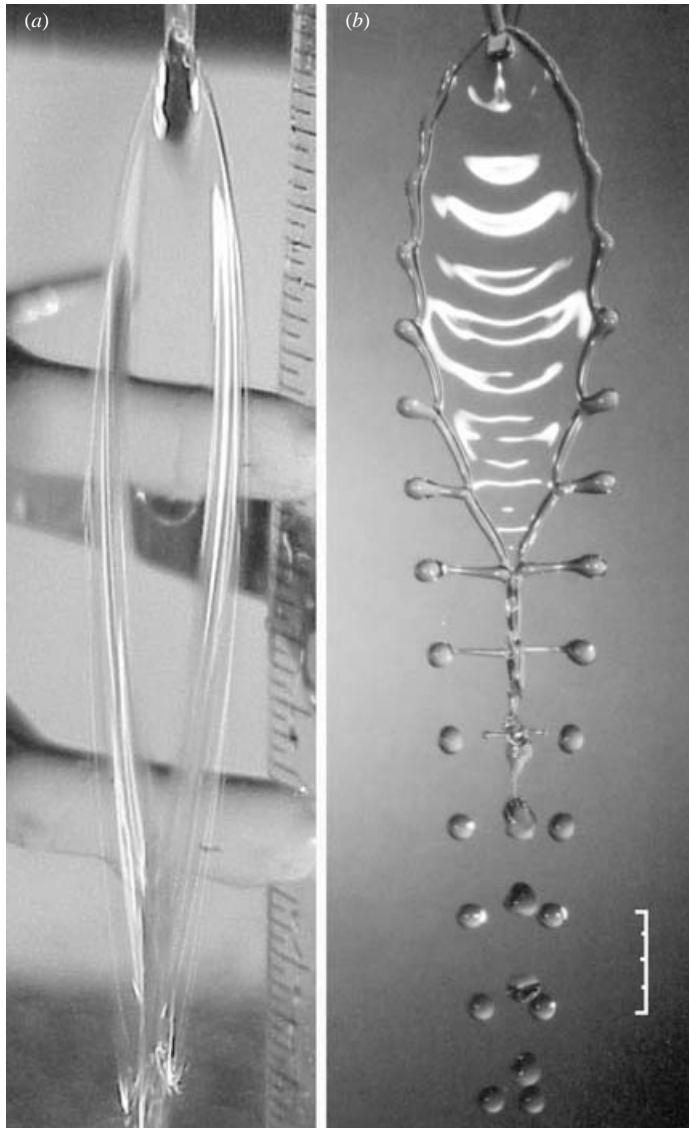


FIGURE 4. The fishbone instability (*a*) An unstable chain link as seen with normal ambient lighting (*b*) Strobe illumination reveals the fishbone form: the fluid sheet corresponds to the fish head, and the tendrils in its wake to the bones. Note the waves on the sheet surface evident in (*b*). Scale bar: 1 cm.

shape of such sheets. The viscous parameter regime examined in our experimental study of colliding fluid jets allows us to test our theory against experiment. Specifically, we integrate the governing equations numerically and compare the calculated shapes with those observed in the laboratory.

In a certain parameter regime, the fluid chain is subject to an instability marked by an apparent blurring of the chain's rim (figure 4*a*). When the flow is illuminated with a strobe lamp, and the frequency of the strobe tuned to that of the flow, one may plainly resolve the details of the flow, which appears to hang motionless in the air (figure 4*b*). Increasing the flow rate broadens the resulting flow structure

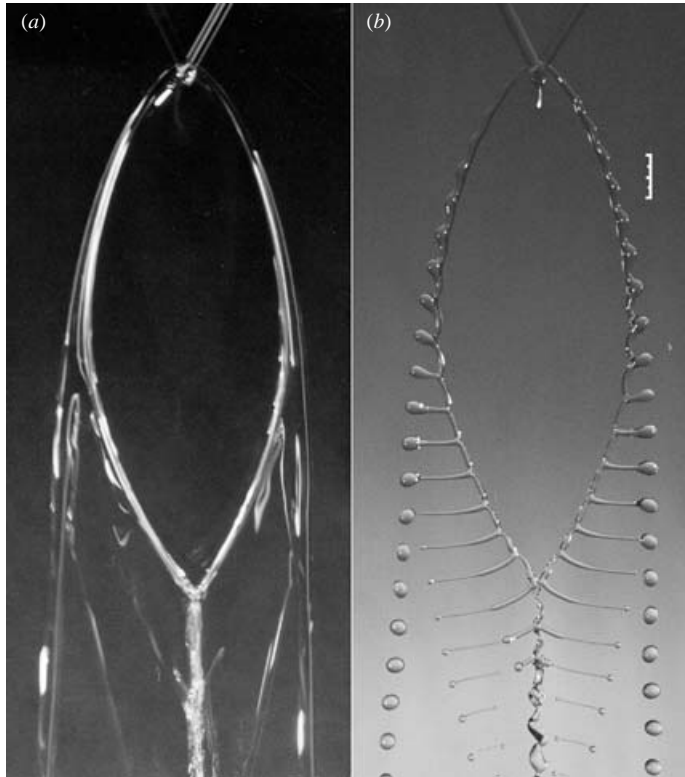


FIGURE 5. The fully developed fishbone structure: (a) with normal ambient lighting it appears blurred, but strobe illumination (b) reveals a broad fishbone structure. Scale bar: 1 cm.

(figure 5), which we refer to as fluid ‘fishbones’: the fish head corresponds to the fluid sheet, and the bones correspond to the underlying fluid tendrils (Hasha & Bush 2002). A consistent physical picture for the fluid fishbones is developed, and a discussion of their stability characteristics presented. The stability is compared to more generic flapping sheet instabilities observed in water (e.g. Dombrowski & Fraser 1954; Ramos 2000; Villermaux & Clanet 2002). We demonstrate that the mechanism for the fishbone instability is quite distinct, with the wavelength being prescribed by the capillary pinch-off of the fluid rims.

In §2, we describe our experimental technique, and in §3 present the results of our experimental study of colliding laminar fluid jets. In §4, we develop the equations governing the shape of a fluid sheet bound by stable rims. In §5, we apply our theory in describing the shape of the first link in the fluid chain, and compare our theoretically predicted shapes with our experiments. The instability of the fluid chain responsible for the fluid fishbones is detailed in §6.

2. Experiments

Our experimental study consists of three components. The first is an exploratory investigation of the flow structures generated from the collision of laminar jets. The second is a careful quantitative study of the form of stable fluid chains, specifically measurements of the form of, and flow within, the first fluid sheet formed by the collision of laminar jets. These measurements are used to test the validity of the

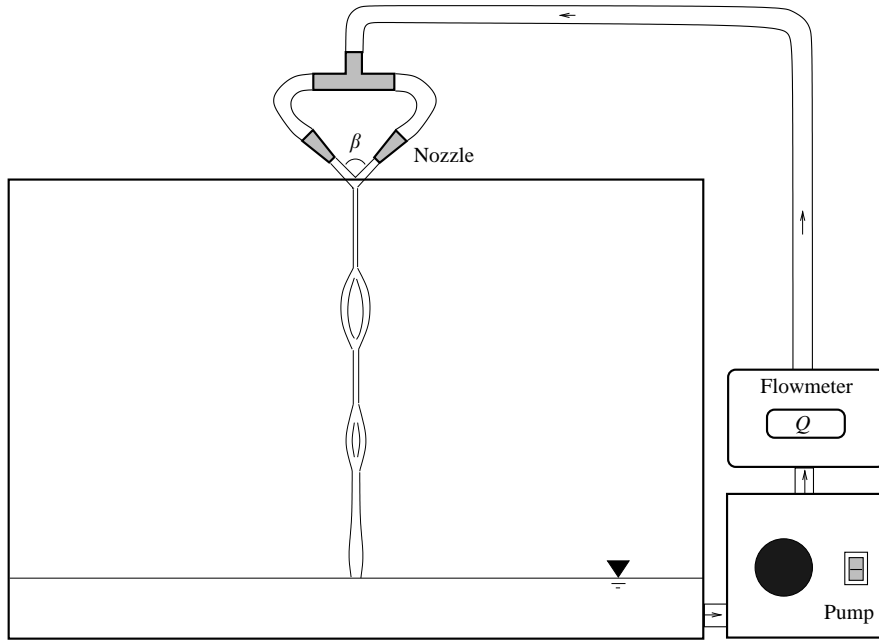


FIGURE 6. A schematic illustration of the experimental apparatus. Glycerol–water solutions were pumped through a pair of identical nozzles with inner radii 0.08 cm, and the flux rates measured with a flowmeter.

theoretical developments for the shapes of fluid sheets bound by stable rims presented in § 4. The third component of our experimental study is an exploration of the fishbone instability.

A schematic illustration of the apparatus used in our experimental study is presented in figure 6. A glycerine–water solution was housed in a square Plexiglas tank with width 50 cm and depth 40 cm. The fluid was pumped from the reservoir through polystyrene tubing into a glass splitter, then through two identical nozzles with inner radius of 0.8 mm to produce a pair of identical fluid jets. Care was taken to ensure that conditions in the tubes after the splitter were symmetric, so that the fluxes in the two jets were identical to an accuracy of 0.5%. The flux in each jet was calculated from the fluid volume expelled into a graduated cylinder over a prescribed time interval. Total flow rates from the variable-flow pump (Cole Parmer, Model 75225-00) were measured with a digital flowmeter (AW Company Model JFC-01) that gave an accuracy of 0.1% over the range considered. Characteristic flow rates are listed in table 1.

The exit nozzles were mounted on adjustable clamps that allowed easy manipulation of the incoming jets. Symmetry in the fluid chains required that the jet centrelines intersect, and was achieved by manipulating the nozzles until the first link lay in the plane perpendicular to the incoming jets, and the second link in the plane of the incoming jets. If the jets were not perfectly aligned, twisting gave the fluid chain a helical form.

Viscosity measurements were made using Cannon-Fenske Routine tube viscometers, that are accurate to 0.14%. Density measurements were made with an Anton-Parr 35N densitometer, that is accurate to 0.01%. Surface tension measurements were made with a Kruss K10 surface tensiometer, that is accurate to 0.1 dyn cm^{-1} .

Parameter	Symbol	Range
Viscosity	ν	0.01–1.0 cm ² s ⁻¹
Density	ρ	1.0–1.2 g cm ⁻³
Surface tension	σ	56–70 dyn cm ⁻¹
Flux rate	Q	4–18 cm ³ s ⁻¹
Incoming jet radii	R_i	0.08 cm
Sheet speed	u_0	100–300 cm s ⁻¹
Jet impact angle	β	30°–180°
Dimensionless group	Definition	Range
We	$\rho u_0^2 R_i / \sigma$	20–300
Re	$u_0 R_i / \nu$	1–2000
Fr	$u_0^2 / (g R_i)$	10 ² –10 ³
S	$Q / (u_0 \pi R_i^2)$	2.0–3.0
Oh	$\sigma R_i / (\mu \nu)$	50–200

TABLE 1. The parameter regime explored in our experimental study of colliding fluid jets.

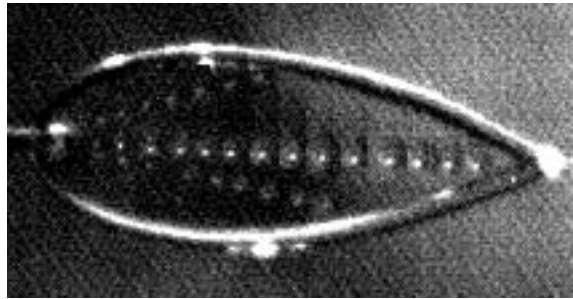


FIGURE 7. A sequence of superimposed frames taken at 500 frames per second with an exposure time of 0.001 s shows the tracks of three bubbles passing through the chain's sheet. Fluid properties: $\nu = 37.6$ cS, $\rho = 1.206$ g cm⁻³, and $\sigma = 61.3$ dyn cm⁻¹. The link length is 5.5 cm. The fluid evidently travels in a straight line from the impact point to the rim. The approximately even spacing of the bubbles between frames indicates the relative constancy of the fluid speed within the sheet. Flow is from left to right.

The frequency of the fishbone instability was measured by synchronizing the flow structure with a digital strobe lamp (Monarch Phaser Strobe) that has a precision of 0.1 Hz. The flow speed and direction within the sheet were measured by particle tracking with a Redlake Motionscope Model PCI 8000S high-speed video camera. Two distinct particle tracking techniques were employed. In the first, plyolite particles with characteristic diameter 50–200 μ m were introduced into the source line, and were visible as they swept through the fluid sheet. In the second, we tracked microbubbles of comparable size that were similarly introduced. As in the experiments of Dombrowski & Fraser (1954), suspended particles with diameters less than the sheet thickness were found to have a negligible influence on the sheet dynamics. In order to ensure that the particle tracks were adequately resolved, we recorded at 500 frames per second with 0.001 second exposure times. These video data were then analysed using Midas Version 2.08 particle tracking software to obtain the sheet velocity field.

Figure 7 illustrates three distinct bubble tracks on a fluid sheet corresponding to a single chain link. The bubble positions are marked every 0.002 s, and indicate that

the sheet velocity is purely radial from the point of impact of the jets. The particle and bubble tracking indicate that the sheet speed is constant to within approximately 10%. We note that this constancy of the sheet speed was assumed but not verified by Taylor (1959*a*), and will be exploited in our theoretical description of the fluid chains presented in §4. The constancy of the speed within a circular sheet was similarly verified by Clanet & Villermaux (2002) using particle tracking. A careful experimental study of the velocity distribution within a fluid sheet formed by the collision of a pair of jets has recently been presented by Choo & Kang (2002), who demonstrated that the sheet speed may decrease with angular distance from its centreline owing to initially non-uniform velocity distributions within the jet that may arise through the influence of the nozzle walls.

The shape of the chain links is expected to depend strongly on the distribution of the flux $Q(\theta)$ within the sheet; however, the theoretical dependence of $Q(\theta)$ on the impact angle of the jets, β , is not simply characterized. Hureau & Weber (1998) develop a theoretical description for the flow generated by the collision of two-dimensional jets; however, the analogous three-dimensional problem has not been solved exactly.

The mirror symmetry of the colliding jets requires that the flux profile be even, and so expressible as a cosine series of the form

$$Q(\theta) = a_0 + a_1 \cos \theta + a_2 \cos 2\theta + \dots$$

Conservation of mass and momentum determine a_0 and a_1 , but the higher-order coefficients are not deduced simply. Conservation of mass, $Q = \int_0^{2\pi} Q(\theta) d\theta$, requires that $a_0 = Q$. Conservation of vertical momentum,

$$2\pi R_i^2 u_i^2 \cos \beta = \int_0^{2\pi} u_0^2 h r \cos \theta d\theta = \int_0^{2\pi} u_0 Q(\theta) \cos \theta d\theta, \tag{2.1}$$

requires that

$$a_1 = SR_i^2 u_i \cos \beta. \tag{2.2}$$

There are an infinite number of possible functional forms $Q(\theta)$ that satisfy these two constraints. The simplest such solution,

$$Q(\theta) = Q + SR_i^2 u_i \cos \beta \cos \theta, \tag{2.3}$$

has been tested experimentally (Miller 1960), but was not found to adequately describe the observed flux profiles. Another solution suggested by Miller (1960) is

$$Q(\theta) = \frac{Q}{2\pi} \left(\frac{1 - \cos^2(\frac{1}{2}\beta)}{1 + \cos^2(\frac{1}{2}\beta)} \right) \left(\frac{1}{1 - \frac{2 \cos(\frac{1}{2}\beta)}{1 + \cos^2(\frac{1}{2}\beta)} \cos \theta} \right). \tag{2.4}$$

This flux profile exhibits more realistic features, such as a small but finite backwards flow for all values of β . It enjoyed a limited success in Miller's experimental study, in which the profile matched experimental observations of a single fluid sheet. However, Miller's profile did not match the profiles observed in our experiments sufficiently well to justify its use in initializing our numerical integrations.

To surmount similar theoretical difficulties, Taylor (1960) was obliged to measure the flux distribution within the sheet by scanning across it with a collection box with a sub-millimetre opening. A similar approach was taken in our experiments: flux profiles were measured by splitting the fluid chains with a razor blade as illustrated in

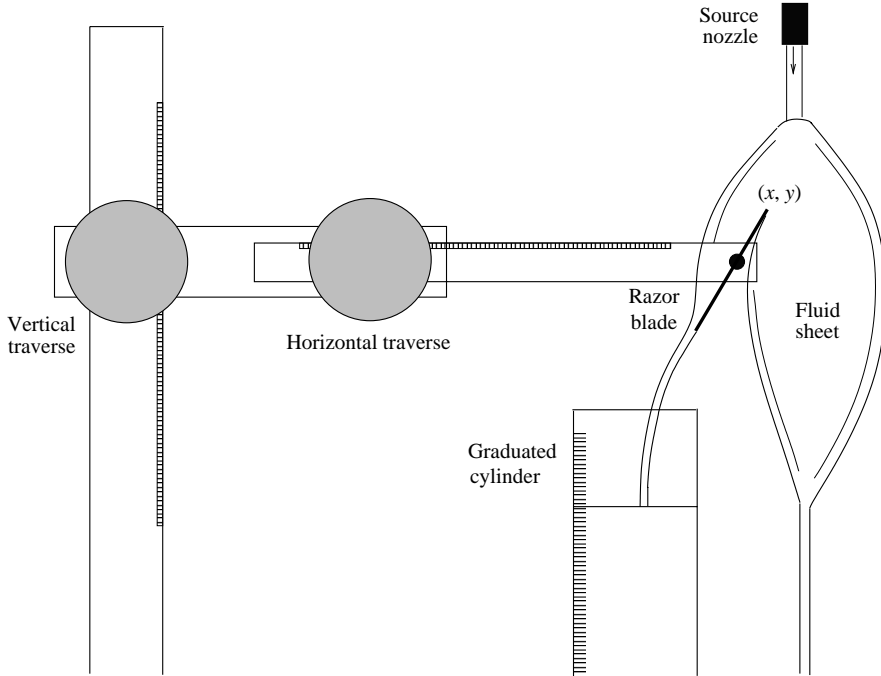


FIGURE 8. The apparatus used to measure flux profiles in the fluid sheets. A razor blade mounted on a vertical and horizontal traverse splits the fluid chain into two streams. Measuring the partition of fluxes in a series of horizontal traverses allows the reconstruction of a flux profile $Q(\theta)$.

figure 8. A razor blade was mounted on a horizontally and vertically adjustable arm. When brought into contact with the thin sheet of the fluid chain and tilted slightly, the razor blade split the chain into two streams. The volume flux was measured by collecting the fluid in each stream with a graduated cylinder and timing with a stop watch. The flux profile within the sheet $Q(\theta)$ was thus reconstructed. We note that the sheet speeds were supercritical (greatly in excess of the capillary wave speed 23 cm s^{-1}); consequently, the measurements did not alter the form of the upstream flux distribution.

The angle between the line joining the tip of the razor blade to the origin and the sheet centreline is defined to be θ (see figure 9). The cumulative volume flux split into the right-hand stream is

$$Q_R(\theta) = \int_{-\pi}^{\theta} Q(\phi) d\phi, \quad (2.5)$$

while that split into the left-hand stream is

$$Q_L(\theta) = \int_{\theta}^{\pi} Q(\phi) d\phi = Q - Q_R(\theta). \quad (2.6)$$

Measurements of Q_L and Q_R were made at various θ values by making horizontal passes across the vertical fluid chain at three different heights. For each pass, horizontal increments of 1 mm were used. For each measurement, the angle θ was computed by recording the razor tip's location (x, y) relative to the origin (see figure 8). The flux distribution $Q(\theta)$ is simply equal to $dQ_R/d\theta$. As the purpose of this study was to test

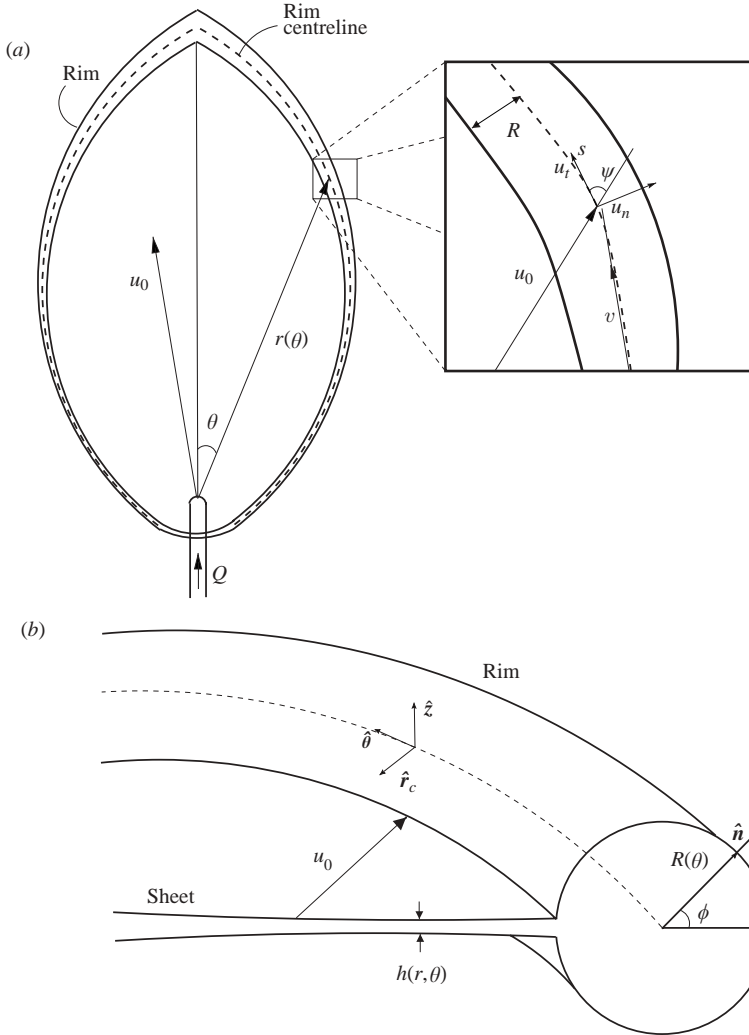


FIGURE 9. A schematic illustration defining the physical variables used in our theoretical description of the fluid chain. (a) A plan view of the first link of the fluid chain. (b) A cross-section of the rim and sheet.

the governing equations of a fluid sheet, and not to solve the problem of colliding jets per se, we chose to fit Miller’s flux profile to the experimental data by treating β as a free variable. Integrating equation (2.4) leads to the cumulative flux profile

$$Q_R(\theta) = \frac{Q}{\pi} \tan^{-1} \left[\left(\frac{1 + \cos(\frac{1}{2}\beta)}{1 - \cos(\frac{1}{2}\beta)} \right) \tan(\frac{1}{2}\theta) \right] + \frac{1}{2}. \tag{2.7}$$

Matlab was used to extract a value of β from the observed data points, and then $Q(\theta)$ as defined in (2.4) was used in the numerical procedures to be detailed in §4. An example of the measured values of $Q_R(\theta)$ for one link is shown in figure 10(a), along with the best-fit curve. The function $Q(\theta)$ computed from these data is shown in figure 10(b). Figure 10(c) illustrates the corresponding sheet thickness profile, as computed a distance 2.76 cm from the point of jet collision.

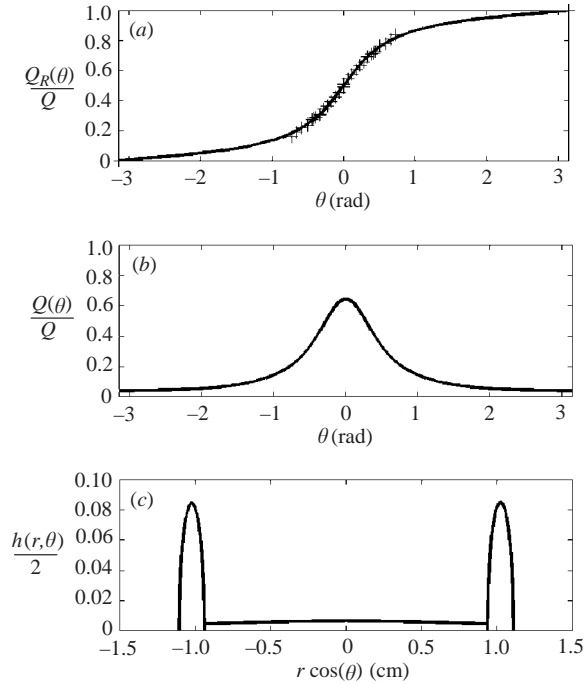


FIGURE 10. (a) The cumulative flux distribution, $Q_R(\theta)$, measured for a sheet generated by two jets with $Q = 10.6 \text{ cm}^3 \text{ s}^{-1}$ colliding at an angle $\beta = 92^\circ$. The resulting sheet is shown in figure 16(b). The error bars are smaller than the extent of the symbols. The solid line indicates the best-fit curve of the form (2.7). (b) The corresponding flux distribution, $Q(\theta)$, of the form (2.4), as calculated from the fitted curve in (a). (c) The corresponding sheet thickness profile, $h(r, \theta)/2$ (cm), a distance 2.76 cm downstream of the origin. Stretching of the vertical coordinate is responsible for the apparent distortion of the circular rims.

3. Observations

Consider two identical jets of radius R_i transporting a total flux Q of fluid of density ρ , kinematic viscosity ν and surface tension σ colliding at an angle β so that the resulting sheet lies in a vertical plane aligned with the gravitational acceleration g . The system is governed by seven physical parameters defined in terms of length, mass, and time. Dimensional analysis thus requires that the system be governed by four dimensionless parameters. The jet Reynolds number $Re_j = Q/(\nu R_i)$ indicates the relative importance of inertia and viscosity in the jet, the jet Weber number $We_j = \rho Q^2/(\sigma R_i^3)$ prescribes the relative importance of inertia and curvature forces, the jet Froude number $Fr_j = Q^2/(g R_i^5)$ indicates the relative importance of inertia and gravity, and β is the impact angle of the colliding jets. Table 1 describes the parameter regime explored in our experimental study. Over the range of viscosities and flow rates examined, the jet Reynolds numbers ranged from 1 to 2000.

The apparatus was oriented so that the fluid chains were vertical. If L is the length of a chain link, and u_0 the mean sheet speed, then gL/u_0^2 indicates the percentage increase in the fluid speed due to gravity as it traverses the chain. For the chains observed, the Froude number was between 0.1 and 0.2, and a maximum acceleration of about 10% could be discerned in the particle tracking measurements. The negligible influence of gravity on the observed flow structures was underscored

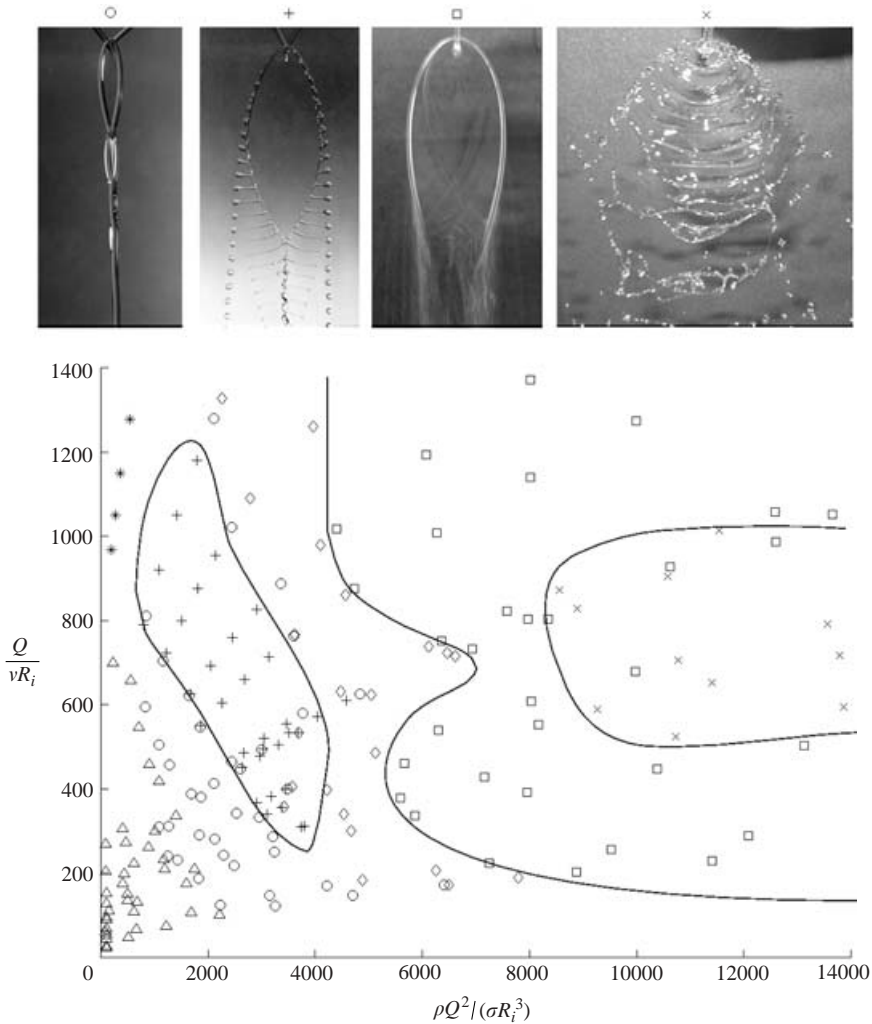


FIGURE 11. Regime diagram illustrating the observed dependence of flow structures emerging from the collision of laminar viscous jets on the governing dimensionless groups. Seven distinct regimes are delineated: Δ , oscillating streams; $*$, sheets with disintegrating rims; O , fluid chains; $+$, fishbones; \diamond , spluttering chains; \square , disintegrating sheets; \times , violent flapping. Glycerine–water solutions with viscosities in the range of 1 to 94 cS were examined.

by our experiments, where it was found that the orientation of the impacting jets (vertical or horizontal) had negligible influence on the initial structure of the resulting flows. In all experiments described henceforth, the fluid sheet resulting from the jet collision was oriented vertically.

Figure 11 is a regime diagram indicating the dependence of the flow structure on the governing parameters Re_j and We_j . For this series of experiments, we fixed the collision angle to be $\beta = \pi/2$, and traced the progression of the flow as the flux was increased for a variety of fluids with viscosities ranging from 1 to 94 cS. Each roughly diagonal trace in figure 11 corresponds to a glycerine–water solution with a different viscosity. The lowermost trace corresponds to the fluid with highest viscosity. The progression of the flow structure for each of the fluids was similar. At the lowest

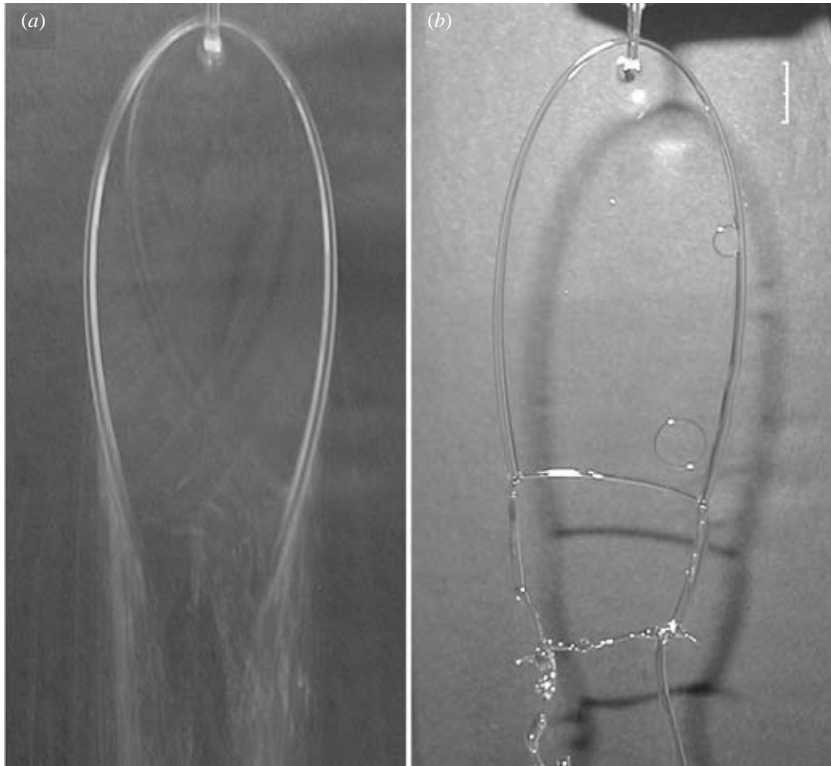


FIGURE 12. The form of the flow taken in the ‘disintegrating sheet’ regime delineated in figure 11. The sheet breaks before the first chain link can close, and is marked by the appearance of expanding holes. (a) A disintegrating sheet under normal ambient lighting. (b) A snapshot of the flow structure. We note that the appearance of the holes may result from the working fluid being a mixture (C. Clanet, personal communication). Scale bar: 1 cm.

flow rates, clear fluid chains do not form: the colliding jets merely coalesce into a single jet marked by inertial–capillary oscillations of the form examined by Rayleigh (1879) and Bohr (1909). The distinction between such oscillations and fluid chains is arbitrary to some degree, but made here on the grounds of the ratio of sheet to rim thickness, which is large for fluid chains. As the flow rate is increased, fully developed chain structures emerge, and the stable chain links increase in length.

When the flow rate exceeds a critical value the fluid chain may be marked by the substantial shortening of the first link and apparent blurring of the rim that accompanies the onset of the fishbone instability. Strobe illumination at the appropriate frequency reveals the perfectly regular and temporally periodic fishbone structure (figures 4 and 5). As the flow rate is increased, the breadth of the fishbone structure increases progressively. The fishbone form persists through a finite range of flux rates, beyond which the sheet reverts to a chain. The resulting chain is considerably longer than that arising prior to the fishbone instability, and is either stable or marked by a weak spluttering of its lower extremities.

As the flux is further increased, the chain becomes unstable, resulting in the irregular disintegration of the sheet into a series of droplets. First, small holes form in the interior of the sheet and spread until they reach the rim, producing fluid ligaments that lead ultimately to a fine spray of droplets (figure 12). At the highest



FIGURE 13. A typical snapshot of the flow taken in the ‘violent flapping’ regime delineated in figure 11. The sheet disintegrates into a series of droplets due to the large-amplitude flapping instability of the sheet. Scale bar: 1 cm.

fluxes considered, the fluid sheet is characterized by a violent flapping instability (figure 13; Dombrowski & Fraser 1954) reminiscent of that on circular water sheets (Clanet & Villermaux 2002), that eventually leads to the break-up of the fluid sheet into a series of microdroplets (Villermaux & Clanet 2002). The parameter regime (figure 11) indicates that the violent flapping instabilities leading to the catastrophic sheet break-up are suppressed by the influence of fluid viscosity.

The leftmost traverse in figure 11 corresponds to water, for which neither chains nor fishbones were observed. The collision of the water jets gave rise to a weakly oscillating stream until a critical flux, beyond which the flow assumed the form of a thin lenticular sheet with unstable rims. This regime corresponds to that examined by Taylor (1960), and is marked by water drops being ejected radially from the sheet’s unstable rims.

We next detail our observations of the fluid fishbones, which yield valuable insight into their origins. The onset of the fishbone structure takes the form of a varicose deformation of the rim at the top of the first link. As the flow rate increases, the sheet length increases and the varicose deformation extends over a greater length of rim and increases in amplitude. Slightly detuning the strobe lamp allows one to observe clearly the evolution of the instability, and reveals that the fishbone instability is accompanied by a flapping of the sheet that grows in amplitude along its length, with a wavelength corresponding to the distance between fishbones. Curvature forces are insufficient to contain the bulbous regions that form along the rim against centripetal forces associated with their curved trajectory along the rim. These bulbous regions are thus flung outwards, drawing out tendrils that are eventually subject to a pinch-off instability that results in a regular array of droplets in the wake of the sheet

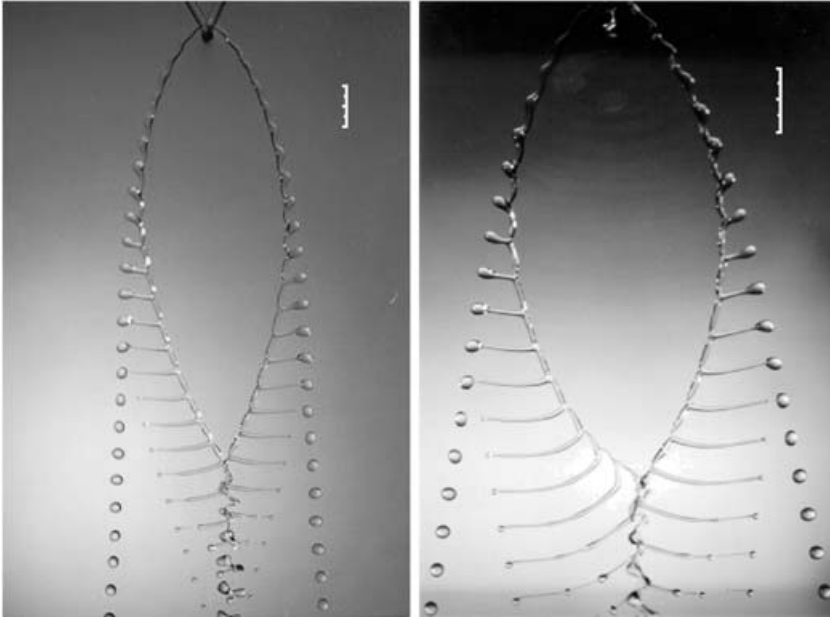


FIGURE 14. Broad fishbone structures resulting from the asymmetric collision of fluid jets.
Scale bars: 1 cm.

(figures 5, 14, 15). The flux of mass and momentum out of the rim has a significant influence on the sheet shape: the first link becomes shorter than its stable counterpart by as much as 50%. This underscores the importance of the flow along the rims to the shape of the sheet, a physical effect treated explicitly in our theoretical developments of §4.

The frequency of the fishbone structure varied from 150 to 250 Hz and, for a particular fluid, was found to increase with increasing flux. The wavelengths were relatively constant over the range considered, varying from 0.7 to 1.0 cm. It is noteworthy that there is hysteresis at the upper limit of the fishbone regime, specifically in approximately the rightmost quarter of the fishbone regime delineated in figure 11: the critical flux at which the fishbones revert to a stable chain is larger when approached from below. In the parameter regime influenced by this hysteresis, the flows are bistable: perturbing the flow by a slight impact with the source jets may cause the structure to change from chains to fishbones, or vice versa. At lower flow rates, the fishbone structure is the only flow observed; no hysteresis was observed at the lower bound of the fluid fishbone regime. The borders marked in figure 11 correspond to those deduced by progressively increasing the flux. Finally, we note that the fluid fishbones were not observed for all fluids, but arose exclusively for fluids with viscosities $5 < \nu < 39.5$ cS. The limited parameter regime ($280 < Re_j < 1200$, $800 < We_j < 4000$) in which the fishbones exist is presumably responsible for their not yet having been reported.

If the jets collide asymmetrically (so that their centrelines do not precisely intersect), a fishbone structure is again observed. In an asymmetric collision, a larger fraction of the horizontal momentum of the jets is transferred directly to the sheet; consequently, the resulting structures are broader than those created by a symmetric collision, and characterized by a more elaborate array of drops downstream, as is evident in figures 14 and 15. The regularity of the fishbone instability is underscored by the fact that the photographs are double exposed, as is evident upon close inspection of

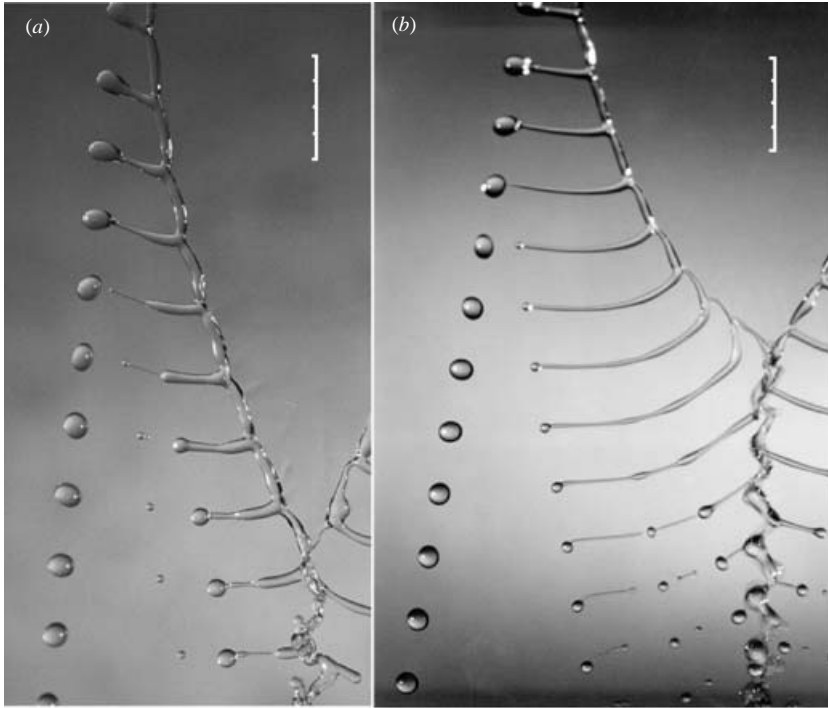


FIGURE 15. Close-ups of the long tendrils of fluid produced by the fishbone instability. As the tendrils pinch-off through the Rayleigh–Plateau mechanism, a regular array of drops is produced in the wake of the fishbones. Scale bars: 1 cm.

the central stream of fluid emerging from the bottom centre of the link in figure 15. The photograph is a superposition of the state of the link at two or more strobe flashes; nevertheless, the delicate flow structure, including that associated with the micropinch-off of the fluid fishbones, is nearly perfectly resolved. Close-ups of the microstructure in the wake of the fluid fishbones are provided in figure 15.

4. Theoretical model of the fluid chain

The centrelines of two identical cylindrical jets of radius R_i with combined volume flux Q collide at the origin. Fluid is ejected radially from the origin into a sheet with flux distribution $Q(\theta)$, so that the volume flux flowing into the sector between θ and $\theta + d\theta$ is $Q(\theta)d\theta$. Guided by the results of our particle tracking experiments, we assume that flow in the sheet has a constant speed u_0 , and is directed purely radially until it reaches the rim of the sheet. Continuity thus requires that the thickness of the fluid sheet, $h(r, \theta)$, decrease like r^{-1} along any ray from the origin.

The relevant geometry is presented in figure 9: $r(\theta)$ is defined to be the distance from the origin to the rim centreline, and $u_n(\theta)$ and $u_t(\theta)$ the normal and tangential components of the fluid velocity in the sheet where it contacts the rim; $v(\theta)$ is defined to be the speed of flow along the rim, $R(\theta)$ the rim radius, and $\psi(\theta)$ the angle between the position vector \mathbf{r} and the local tangent to the rim centreline. Finally, $r_c(\theta)$ is defined to be the radius of curvature of the rim centreline, and s the arc length along the rim centreline. The differential equations governing the shape of a steady stable fluid rim bounding a fluid sheet may be deduced by consideration of

conservation of mass in the rim and the local normal and tangential force balances at the rim (Taylor 1959a).

Continuity requires that the tangential gradient in volume flux along the rim be balanced by the flux entering the rim from the sheet:

$$\frac{\partial}{\partial s}(v\pi R^2) = u_n h. \quad (4.1)$$

In the case of unstable rims, such as those arising in the fishbone instability, an additional sink term would be required to account for the mass ejected by instability (e.g. Clanet & Villermaux 2002); however, we here restrict our attention to the case of steady stable fluid rims as arise in the fluid chains.

The normal force balance requires that the curvature force associated with the rim's surface tension balance the force resulting from the normal flow into the rim from the sheet and the centripetal force resulting from the flow along the curved rim. By assuming that the rims are circular in cross-section, that $R/r_c \ll 1$, and that the rim radius is large relative to the sheet thickness, we deduce in the Appendix an explicit expression for the curvature force (A 6). The normal force balance thus assumes the form

$$\rho u_n^2 h + \frac{\rho \pi R^2 v^2}{r_c} = 2\sigma + \frac{2\sigma(\pi - 1)R}{r_c}. \quad (4.2)$$

Note that the curvature force has two components. The first, 2σ , is that associated with the curvature in a plane perpendicular to the fluid sheet and normal to the rim. The second, $2\sigma(\pi - 1)R/r_c$, is that associated with the curvature of the rim centreline.

The tangential force balance at the rim requires that tangential gradients in tangential momentum flux be balanced by tangential gradients in curvature pressure, viscous resistance F_v , and the tangential momentum flux arriving from the sheet:

$$\rho \frac{\partial}{\partial s}(\pi R^2 v^2) = -\pi R^2 \sigma \frac{\partial}{\partial s} \overline{\nabla \cdot \hat{n}} + F_v + \rho h u_t u_n. \quad (4.3)$$

The relative magnitudes of the inertial and viscous terms is prescribed by the rim Reynolds number $u_0 R/\nu$, which assumes a minimum of $O(10^2)$: in our system, the influence of viscosity may be safely neglected. Accurate to $O(R/r_c)$, we express the mean curvature as $\overline{\nabla \cdot \hat{n}} = 1/R$. The steady tangential force balance may thus be expressed

$$\frac{\partial}{\partial s}(\pi R^2 v^2) = h u_t u_n - \frac{\pi R^2 \sigma}{\rho} \frac{\partial}{\partial s} \left(\frac{1}{R} \right). \quad (4.4)$$

It is valuable to compare our governing equations with those deduced by Taylor (1959b). Our analysis differs from that of Taylor only through inclusion of terms associated with a finite rim radius. In the normal stress balance, Taylor neglected the term resulting from the curvature of the rim centreline. In the tangential force balance, he neglected the pressure term resulting from tangential gradients in rim curvature. While these terms are small (of order R/r_c and We^{-1} , respectively) in our application, physical settings may arise where they are non-negligible; consequently, we retain them for the sake of generality.

We proceed by reducing (4.1), (4.2), and (4.4) to a system of partial differential equations in terms of $r(\theta)$, $v(\theta)$, $R(\theta)$, and $\psi(\theta)$, as well as the empirically deduced flux function $Q(\theta)$. Conservation of mass in the sheet requires

$$h = \frac{Q(\theta)}{u_0 r}. \quad (4.5)$$

Geometry indicates that

$$ds^2 = dr^2 + (r d\theta)^2 \tag{4.6}$$

and

$$\frac{dr}{d\theta} = r \cot \psi. \tag{4.7}$$

Thus,

$$ds = \frac{r d\theta}{\sin \psi} \quad \text{and} \quad \frac{d}{ds} = \frac{\sin \psi}{r} \frac{d}{d\theta}. \tag{4.8}$$

We also employ the geometric relations:

$$u_n = u_0 \sin \psi, \quad u_t = u_0 \cos \psi, \tag{4.9}$$

$$\frac{1}{r_c} = \frac{d}{ds}(\psi + \theta) = \frac{\sin \psi}{r} \left(\frac{d\psi}{d\theta} + 1 \right). \tag{4.10}$$

Substituting into equations (4.1), (4.2) and (4.4) yields

$$Q(\theta) = \frac{d}{d\theta}(v\pi R^2), \tag{4.11}$$

$$\rho u_0 Q(\theta) \sin^2 \psi + \rho \pi R^2 v^2 \sin \psi \left(\frac{d\psi}{d\theta} + 1 \right) = 2\sigma \left(r + (\pi - 1)R \sin \psi \left(\frac{d\psi}{d\theta} + 1 \right) \right), \tag{4.12}$$

$$\frac{d}{d\theta}(\pi R^2 v^2) = Q(\theta) u_0 \cos \psi + \frac{\pi \sigma}{\rho} \frac{dr}{d\theta}. \tag{4.13}$$

These equations, together with (4.7), completely characterize the dynamics of the stable rims.

We introduce dimensionless variables, designated by stars, as follows:

$$(u_t, v) = u_0(u_t^*, v^*), \quad R = R_i R^*, \quad r = (\rho u_0 Q / 2\sigma) r^*, \quad Q(\theta) = Q q(\theta), \tag{4.14}$$

where R_i is the radius of the impacting jets, Q the total jet flux, u_0 the sheet speed and $\rho u_0 Q / (2\sigma)$ the Taylor radius. Substituting into equations (4.11)–(4.13) and dropping stars yields the dimensionless rim equations:

$$\frac{d}{d\theta}(v R^2) = S q(\theta), \tag{4.15}$$

$$q(\theta) \sin^2 \psi + \frac{1}{S} R^2 v^2 \sin \psi \left(\frac{d\psi}{d\theta} + 1 \right) = r + \frac{1}{WeS} \frac{2(\pi - 1)}{\pi} R \sin \psi \left(\frac{d\psi}{d\theta} + 1 \right), \tag{4.16}$$

$$\frac{d}{d\theta}(R^2 v^2) = S q(\theta) \cos \psi + We^{-1} \frac{dr}{d\theta}. \tag{4.17}$$

The system is uniquely prescribed by the three dimensionless groups

$$S = \frac{Q}{u_0 \pi R_i^2}, \quad We = \frac{\rho u_0^2 R_i}{\sigma}. \tag{4.18}$$

The range of these parameters in our experimental study is detailed in table 1.

Rearranging the equations yields the following system of differential equations:

$$\frac{dr}{d\theta} = r \cot \psi, \quad (4.19)$$

$$\frac{d\psi}{d\theta} = \frac{S(r - q(\theta) \sin^2 \psi)}{R^2 v^2 \sin \psi - We^{-1} [2(\pi - 1)/\pi] R \sin \psi} - 1, \quad (4.20)$$

$$\frac{dr}{d\theta} = Sq(\theta) \frac{2v - \cos \psi}{(2Rv^2 + We^{-1})}, \quad (4.21)$$

$$\frac{dv}{d\theta} = Sq(\theta) \frac{We^{-1} - 2Rv^2 + 2Rv \cos \psi}{2R^3 v^2 + R^2 / We}. \quad (4.22)$$

When appropriately initialized (in a manner to be detailed in §5), this system may be integrated to yield the shape of a fluid sheet bound by stable rims, specifically the first link in the fluid chain.

5. Comparison of experiments and theory

To calculate the sheet shapes corresponding to the first link in the stable fluid chains, the flux profile $Q(\theta)$ and constant sheet speed u_0 were measured using the techniques detailed in §2, and used as input to the theory detailed in §4. The numerical integration of equations (4.19)–(4.22) was initialized at a point on the rim corresponding to the largest angle θ_0 for which a point on the cumulative flux profile was measured. At this point, the initial conditions, specifically the variables $r(\theta_0)$, $\psi(\theta_0)$, $R(\theta_0)$ and R_i , were measured from a chain image in Matlab's Image Processing Toolbox. The appropriate lengthscale was deduced from a reference length, a millimetre grid, included in the image. The initial rim speed $v(\theta_0)$ was calculated from the measured rim radius and flux profile: as the flux in the rim at θ_0 is $Q_R(\theta_0)$, the rim speed is given by

$$v(\theta_0) = Q_R(\theta_0) / (\pi R(\theta_0)^2). \quad (5.1)$$

Figure 16 shows overlays of three observed and theoretically predicted chain link shapes. The grid lines in the numerical curves are separated by 2 cm. The output of the numerics was fit to the photographs by matching these grid lines to the reference lengthscale, then positioning the origin of the model at the centre of the jet impact region. The theoretical curves produce a satisfactory prediction of the observed chain link shape for each trial.

The primary source of error arises from inaccuracy in the flux profile measurements. In calculating these profiles, the vertical and horizontal distances from the tip of the razor to the point of collision of the jets were measured at increments of 1 mm, with an accuracy of 0.2 mm. The error in the inferred flux introduced by this inaccuracy could be as large as 20%, but was typically on the order of 5–10%. Moreover, these errors were minimized through correlating the flux profiles inferred along each of the three horizontal passes. Systematic error in the angle measurements could also be introduced through misalignment, specifically if the chain was not perfectly vertical or if the traverse arm holding the razor was not parallel to the fluid sheet. The resulting misalignment error was most pronounced when the vertical distance from the razor tip to collision point was small. However, the systematic error so produced was easily identified, and the data from such flawed trials were discarded. In practice, the spread in the flux profile data was within 10%, and the measured flux profiles were adequate to produce a satisfactory agreement between theory and experiment.

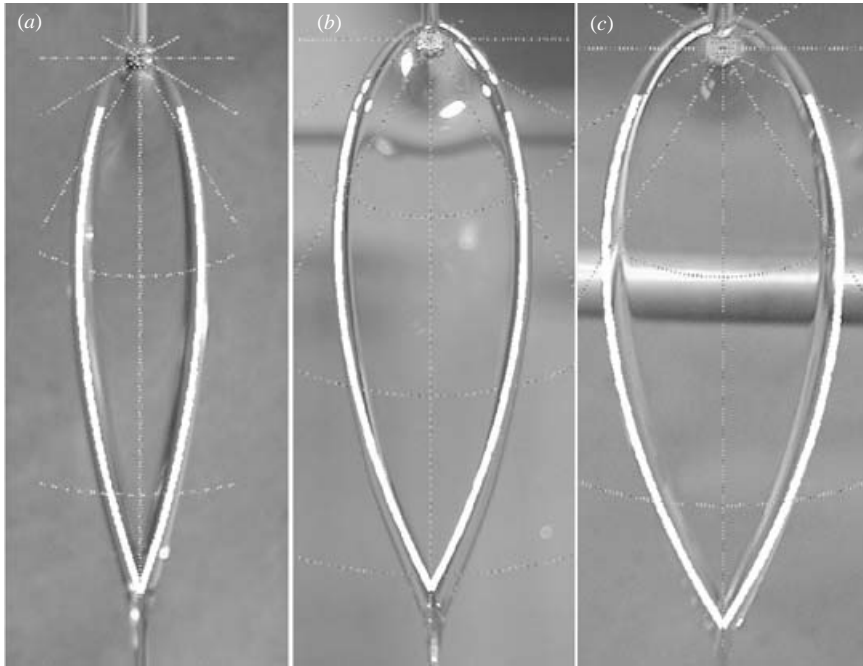


FIGURE 16. Comparisons of observed and theoretically predicted (white lines) shapes of the sheets comprising the first chain link. (a) $We = 58.6$, $Re = 38.56$, $Q = 10.1 \text{ cm}^3 \text{ s}^{-1}$, $\beta = 44^\circ$. (b) $We = 58.8$, $Re = 40.4$, $Q = 10.6 \text{ cm}^3 \text{ s}^{-1}$, $\beta = 92^\circ$. (c) $We = 40.0$, $Re = 33.0$, $Q = 9.21 \text{ cm}^3 \text{ s}^{-1}$, $\beta = 135^\circ$. The grid arcs are 2 cm apart.

In the parameter space examined experimentally, a maximum acceleration of about 10% could be discerned in the particle tracking measurements. For the numerics, the sheet speed was taken as the average value measured experimentally. The influence of aerodynamic drag on fluid sheets was examined by Taylor (1959a), whose analysis may be directly applied to our model. The estimated percentage loss of sheet speed due to air drag was calculated; in all cases, the correction to the sheet speeds was of order 10^{-3} , and so safely neglected.

Finally, we note that care had to be taken in measuring surface tension, to which the predicted sheet shapes were extremely sensitive. It was necessary to make surface tension measurements directly following an experiment, as the surface tension of the glycerine–water solutions was found to be weakly time-dependent (varying by up to 5% over the course of a week). Presumably this weak time-dependence was the result of some combination of evaporation, uptake of water vapour from the atmosphere, and diffusion of soluble surfactant to the surface.

6. Fishbones

Fluid fishbones are characterized by two coupled physical effects: the varicose instability on the rim, and the flapping of the fluid sheet. Both sheet- and rim-driven instabilities were thus considered as instigators of the fishbones. The fishbones may be the result of a shear-induced flapping wave mode excited on the fluid sheet (Squire 1953; Hagerty & Shea 1955): the flapping mode disrupts the flow in the rim, leading to the formation of the bulbous regions that are flung outwards by the centripetal force, and drawn into the tendrils that comprise the fishbones. The linear stability theory

for a flapping fluid sheet predicts a most unstable wavelength that is larger than that observed by an order of magnitude (Squire 1953). Moreover, figure 11 clearly indicates that fishbones exist only in a finite range: for a particular fluid, they vanish at both higher and lower flux rates. This is inconsistent with the view that the fishbones are initiated by a shear-induced flapping instability: such flapping sheets are not expected to revert to a stable form as flow rates are increased (Clark & Dombrowski 1972; Crapper, Dombrowski & Pyott 1975). It is noteworthy that the classical flapping sheet regime was observed in our experiments (at the right in figure 11), but at considerably higher flow rates. We thus conclude that the fishbone instability is rim- rather than sheet-driven.

Two possibilities exist for rim-driven instabilities on the fluid sheet. First, the fishbones may be prompted by a Rayleigh–Taylor instability induced by the centripetal accelerations associated with flow along the curved rim. Second, the driving mechanism may be the capillary instability of the rim: the Rayleigh–Plateau instability (Rayleigh 1879) prompts rim pinch-off; the subsequent distortion is amplified by the centripetal forcing associated with flow along the curved rim. According to either of these physical pictures, the waves evident on the fluid sheet are generated by the disruption of the sheet forced by the rim break-up, and so are not instrumental in setting the wavelength of instability. We proceed by investigating the relative importance of the Rayleigh–Taylor and Rayleigh–Plateau mechanisms.

Consider an interface, across which there is a density difference ρ , accelerating at a rate a_c normal to the interface. The Rayleigh–Taylor instability will induce instability of all modes with wavelength $\lambda > 2\pi(\sigma/(\rho a_c))^{1/2}$. The most unstable mode has a wavelength $2\sqrt{3}\pi(\sigma/(\rho a_c))^{1/2}$ and timescale of instability $(\frac{2}{3}/\sqrt{3})(\sigma/(\rho a_c^3))^{1/4}$ (Chandrasekar 1961). In our study, a Rayleigh–Taylor-type instability may be induced on the sheet's rim by the centripetal acceleration, $a_c = v^2/r_c$ associated with flow along the curved rim. The Rayleigh–Taylor mechanism thus predicts wavelengths of instability and growth rates that depend explicitly on the magnitude of the centripetal acceleration and so the rim speed; specifically, the wavelength of the most unstable mode is proportional to $1/v$. The magnitude of the centripetal acceleration in our sheets was computed in §4, and found to vary substantially, both between experiments and along the length of a single rim, between a minimum of 0 at the stagnation point at the top of the chain and a maximum of approximately 3000 cm s^{-2} . One thus expects that the Rayleigh–Taylor mechanism for rim instability would generate a wide range of wavelengths with a minimum of 1.2 cm. In our experimental study, the wavelength of instability was found to vary over an extremely limited range, 0.7–1.0 cm.

The form of Rayleigh–Plateau pinch-off of a fluid thread of radius R is prescribed by the Ohnesorge number, $Oh = \sigma R/(\mu v)$, a Reynolds number based on the capillary wave speed σ/μ (Weber 1931; Chandrasekhar 1961; Eggers 1997). At high Oh , the pinch-off is resisted by fluid inertia, and the most unstable mode has a wavelength of $9.02R$ and timescale of instability $2.91(\rho R^3/\sigma)^{1/2}$. At low Oh , the pinch-off is resisted by fluid viscosity, the instability shifts to long wavelengths, there is no finite mode of maximum instability, and the timescale of instability is $\mu R/\sigma$. The fluid rims in our problem have characteristic diameter of 1–2 mm and an Ohnesorge number of $O(100)$; consequently, the high- Oh results are relevant. The spacing between bones was found to lie between 0.7 and 1.0 cm in all the experiments considered, and so to be consistent with a Rayleigh–Plateau mechanism for pinch-off. Furthermore, we note that the rim instability is initiated very close to the top of the chain, where the centripetal acceleration is smallest, so the Rayleigh–Taylor mechanism would predict the slowest growing modes and longest wavelengths.

The constancy of the wavelength of instability in our experiments indicates that the Rayleigh–Plateau mechanism is responsible for the fishbones. Using parameters appropriate for the sheet rim (table 1) indicates that the timescale of capillary pinch-off, $\tau \sim (R^3 \rho / \sigma)^{1/2} \sim 0.01$ s, is comparable to the time required for a fluid parcel to traverse the chain. This offers a plausible explanation for the reversion from fishbones to stable chain structures at high flow rates: the flow speed must be sufficiently low that the instability has time to develop. A fishbone criterion based on this simple physical picture is discussed in § 7.

Structures reminiscent of the fluid fishbones have been generated by acoustic forcing at the source of spray atomizers (Van Dyke 1988, p. 87). The possibility that fishbones were forced by some resonance in our system was carefully considered. The fishbone structure still obtains when the jets are produced by a gravity feed; we thus ruled out pump vibrations as the source of instability. We similarly ruled out other parts of the apparatus by replacing them with different components; the fishbone instability was robust to all such changes.

7. Discussion

The reduced equations, (4.1)–(4.4), prescribe the shape of fluid sheets bound by stable rims. The system is a generalization of that developed by Taylor (1959*b*) through inclusion of the curvature force associated with the bending of the rim, and the pressure force associated with tangential gradients in rim radius. In the parameter regime considered in our experiments, these new terms are not significant; consequently, our governing equations reduce to those of Taylor (1959*b*). Nevertheless, our experimental study has provided a successful test of these equations in a new and relatively simple geometry. Clanet & Villermaux (2002) used these equations to predict successfully the distortion of a circular horizontal sheet by its impact with a vertical wire, a geometry originally investigated qualitatively by Taylor (1959*a*). In Taylor's (1960) investigation of colliding jets, the sheets were generated with water, the rims were unstable, and sheet shapes were simply prescribed by the Taylor radius $\rho u_0 Q(\theta) / (2\sigma)$. By increasing the viscosity of our test fluid, we were able to access and investigate the parameter regime characterized by stable rims, in which the sheet shape is strongly influenced by centripetal forces associated with flow along the rim.

We have examined the rich family of flow structures generated by the collision of high-Reynolds-number laminar viscous jets. The flow forms observed are summarized in figure 11, and include the fluid chains and fishbones that have been the principal focus of our study. The detailed stability analysis required to predict the bounds between the various flow regimes delineated in figure 11 is left as a subject for future consideration. We here simply discuss the mechanisms responsible for the observed instabilities. First, the violent shear-induced flapping instabilities (figure 13) of the sheet arising at the highest flow rates have been considered in detail by previous investigators (Dombrowski & Fraser 1954; Mehring & Sirignano 1999; Villermaux & Clanet 2002), and so have only been touched upon in our study. Second, the transition from the spluttering chains to the disintegrating sheet (figure 12) is expected to arise when the sheet length exceeds the Taylor radius. One thus expects this transition to be independent of Re_j , and so to be represented by a vertical line in figure 11, as is roughly the case for $Re_j > 800$.

The fluid chains and fishbones represent a class of flows dominated by fluid inertia and surface tension; nevertheless, fluid viscosity evidently plays a critical role in their form through its influence on the rim size and stability. Figure 11 indicates that for

$Re_j > 800$, the fishbones represent an intermediate state between the water sheets (with unstable rims) studied by Taylor (1960) and the fluid chains (with stable rims). The fishbones may thus be viewed as a manifestation of viscosity regularizing the instability of the fluid rim. The presence of a minimum Reynolds number (approximately 280) below which fishbones do not exist similarly suggests the importance of fluid viscosity in suppressing the capillary instability of the rims. The finite window of fluid viscosities in which the fishbones arise may thus be rationalized: the viscosity must be sufficiently high that the rapid rim instability observed by Taylor (1960) not arise, and sufficiently low that the rim not be entirely stable (as in the case of the chains).

It is generally expected that the fluid chains will replace the fishbones when the growth time of the capillary instability of the bounding rim τ_p is exceeded by the travel time along the rim. For a sheet of length L and speed u_0 the convective timescale is $\tau_c = L/u_0$. While in general τ_p will depend on fluid viscosity, for an inviscid sheet bound by rims of radius R , the timescale of capillary pinch-off at high Oh is $\tau_p = 2.91(\rho R^3/\sigma)^{1/2}$ (Chandrasekhar 1961). The onset of the fishbone instability in the inviscid limit thus requires that

$$\frac{\tau_p}{\tau_c} \sim \frac{R}{L} \left(\frac{R}{R_i} \right)^{1/2} We^{1/2} < 1. \quad (7.1)$$

If R and L were independent of Re_j and We , one would expect the fishbones to arise for all Weber numbers below a critical value; however, one expects a nonlinear dependence of $R^{3/2}/(LR_i^{1/2})$ on Re_j and We . Clanet & Villermaux (2002) demonstrated that the mean rim size of a circular sheet decreases with increasing Weber number. While our sheet geometry is different, such a trend in our system would be consistent with the observed finite extent of the fishbone regime; specifically, it would decrease the likelihood of τ_p/τ_c being a monotonically increasing function of Q .

A fishbone criterion expressible in terms of the source conditions would require a more complete understanding of the dependence of the rim radius and instability on Re_j and We . The linear theory for the Rayleigh–Plateau instability (Chandrasekhar 1961) indicates that in the parameter regime examined in our study ($Oh \sim 50 - 200$), viscosity is expected to increase the timescale of capillary pinch-off by a factor of 1.5–3 relative to that for the inviscid case, thus providing some rationale for the observed dependence on Re_j of the boundary between chains and fishbones. Finally, we note that in our system the rim radius necessarily increases with distance along the rim; the tendency of rim growth to suppress the capillary instability has recently been demonstrated by Fullana & Zaleski (1999). A more detailed investigation of criteria for the fishbone instability will be the subject of future consideration.

The generic picture of droplet formation from high-speed fluid sheets was originally presented by Dombrowski & Johns (1963), and has been refined by Villermaux & Clanet (2002). The sheet becomes unstable to a flapping mode instability that eventually leads to the sheet breaking up into a series of fluid ligaments aligned perpendicular to the flow direction. Subsequently, the ligaments break into a series of droplets via the Rayleigh–Plateau pinch-off mechanism. We note that droplet formation accompanying the fishbone instability is inherently different, being rim-rather than sheet-based. While the latter stages of the fishbone instability are similarly characterized by the capillary pinch-off of fluid ligaments, these ligaments arise from the coupling of the capillary pinch-off of the fluid rims with the centripetal forcing associated with flow along the rims.

The authors thank Tom Peacock, Jeff Leblanc and Jeff Aristoff for their assistance with the experiments. We also gratefully acknowledge Gareth McKinley and José Bico for granting us access to their surface-tensiometer. Finally, we thank Christophe Clanet, Michael Brenner, Tom Peacock and Howard Stone for a number of valuable discussions. J.W.M.B. gratefully acknowledges the financial support of an NSF Career Grant CTS-0130465. A.E.H. was supported by MIT's UROP Program.

Appendix. The curvature force on the sheet's rim

We here deduce an expression for the curvature force per unit length, F_c , acting on the sheet's rim. We denote by \hat{n} the unit vector normal to the rim surface and by s the local tangent to the rim centreline, and assume the sheet lies in a horizontal plane (refer to figure 9). One may generally express the curvature force acting over a surface S as

$$F_c = \int_S \sigma (\nabla \cdot \hat{n}) d\hat{S}. \tag{A 1}$$

An expression for the curvature $J = \nabla \cdot \hat{n}$ may be obtained by assuming that the cross-section of the rim is circular in the vertical plane parallel to the local radius of curvature. J may then be characterized entirely by the radius of curvature r_c of the centreline and the derivatives of the rim radius R with respect to θ . We compute the curvature of the surface defined by the position vector:

$$\mathbf{T}(\theta, \phi) = (\cos \theta [r_c + R(\theta) \cos \phi], \sin \theta [r_c + R(\theta) \cos \phi], R(\theta) \sin \phi), \tag{A 2}$$

that corresponds locally to a tapered cylindrical section:

$$J = -\frac{(r_c + 2R \cos \phi)}{R(r_c + R \cos \phi)} - \frac{(dR/d\theta)^2(3R \cos \phi + r_c) - (d^2R/d\theta^2)(R^2 \cos \phi + Rr_c)}{R((r_c + R \cos \phi)^2 + (dR/d\theta)^2)^{3/2}}. \tag{A 3}$$

In the limit of $R^2/r_c^2 \ll 1$, the second term is negligible, so we obtain

$$J = -\frac{r_c + 2R \cos \phi}{R(r_c + R \cos \phi)}, \tag{A 4}$$

which corresponds to the total curvature of a torus of inner radius R and outer radius r_c .

To compute the surface integral required for the curvature force per unit length (A1), we use the local coordinate system defined by the unit vectors \hat{r}_c, \hat{z} , and $\hat{\theta}$; \hat{r}_c is the normal to the rim centreline in the plane of the sheet, \hat{z} the vertical and $\hat{\theta}$ the tangent to the rim centreline. Substituting $d\hat{S} = R d\phi (r_c + R \cos \phi) \hat{n} d\theta$ and (A 4) into (A 1) yields the curvature force per unit length along the rim, accurate to $O((R/r_c)^2)$:

$$F_\sigma = \frac{2\sigma(r_c - R)}{r_c} \hat{r}_c + \frac{\sigma}{r_c} \int_{-\pi}^{\pi} (r_c + 2R \cos \phi) (\cos \phi \hat{r}_c + \sin \phi \hat{z}) d\phi \tag{A 5}$$

$$= 2\sigma \left(\frac{r_c - R}{r_c} + \frac{\pi R}{r_c} \right) \hat{r}_c. \tag{A 6}$$

REFERENCES

BAYVEL, L. & ORZECOWSKI, Z. 1993 *Liquid Atomization*. Taylor and Francis.
 BOHR, N. 1909 Determination of the surface-tension of water by the method of jet vibration. *Phil. Trans. R. Soc. Lond. A* **209**, 281–317.

- BUCKINGHAM, R. & BUSH, J. W. M. 2001 Fluid polygons. *Phys. Fluids: Gallery of Fluid Motion* **13**, S10.
- CHANDRASEKHAR, S. 1961 *Hydrodynamic and Hydromagnetic Stability*. Dover.
- CHOO, Y.-J. & KANG, B.-S. 2002 The velocity distribution of the liquid sheet formed by two low-speed impinging jets. *Phys. Fluids* **14**, 622–627.
- CLANET, C. & VILLERMAUX, E. 2002 The life of a smooth liquid sheet. *J. Fluid Mech.* **462**, 307–340.
- CLARK, C. J. & DOMBROWSKI, N. 1972 Aerodynamic instability and disintegration of inviscid liquid sheets. *Proc. R. Soc. Lond. A* **329**, 467–478.
- CRAPPER, G. D., DOMBROWSKI, N. & PYOTT, G. 1975 Large amplitude Kelvin-Helmholtz waves on thin liquid sheets. *Proc. R. Soc. Lond. A* **342**, 209–224.
- DOMBROWSKI, N. & FRASER, R. P. 1954 A photographic investigation into the disintegration of liquid sheets. *Phil. Trans. R. Soc. Lond. A* **247**, 101–130.
- DOMBROWSKI, N. & JOHNS, W. 1963 The aerodynamic instability and disintegration of liquid sheets. *Chem. Engng Sci.* **18**, 203–214.
- EGGERS, J. 1997 Nonlinear dynamics and breakup of free surface flows. *Rev. Mod. Phys.* **69**, 865–929.
- FULLANA, J. M. & ZALESKI, S. 1999 Stability of a growing end rim in a liquid sheet of uniform thickness. *Phys. Fluids* **11**, 952–954.
- HAGERTY, W. W. & SHEA, J. F. 1955 A study of the stability of plane fluid sheets. *J. Appl. Mech.* **22**, 509–515.
- HASHA, A. E. & BUSH, J. W. M. 2002 Fluid fishbones. *Phys. Fluids: Gallery of Fluid Motion* **14**, S8.
- HUREAU, J. & WEBER, R. 1998 Impinging free jets of ideal fluid. *J. Fluid Mech.* **372**, 357–374.
- JOHNSON, M. F., MIKSIĆ, M. J., SCHLUTER, R. J. & BANKOFF, S. G. 1996 Fluid chains produced by obliquely intersecting viscous jets connected by a thin free liquid film. *Physics of Fluids: Gallery of Fluid Motion* **8**, S2.
- LEFEBVRE, A. H. 1989 *Liquid Atomization*. Hemisphere.
- MEHRING, C. & SIRIGNANO, W. A. 1999 Nonlinear capillary wave distortion and disintegration of thin planar liquid sheets. *J. Fluid Mech.* **388**, 69–113.
- MILLER, K. D. 1960 Distribution of spray from impinging liquid jets. *J. Appl. Phys.* **31**, 1132–1133.
- RAMOS, J. I. 2000 Asymptotic analysis and stability of inviscid liquid sheets. *J. Math. Anal. Appl.* **250**, 512–532.
- RAYLEIGH, LORD 1879 On the capillary phenomena of jets. *Proc. R. Soc. Lond.* **29**, 71–97.
- SQUIRE, H. B. 1953 Investigation of the instability of a moving liquid film. *Brit. J. Appl. Phys.* **4**, 167–169.
- TAYLOR, G. I. 1959*a* The dynamics of thin sheets of fluid ii: Waves on fluid sheets. *Proc. R. Soc. Lond. A* **253**, 296–312.
- TAYLOR, G. I. 1959*b* The dynamics of thin sheets of fluid iii: Disintegration of fluid sheets. *Proc. R. Soc. Lond. A* **253**, 313–321.
- TAYLOR, G. I. 1960 Formation of thin flat sheets of water. *Proc. R. Soc. Lond. A* **259**, 1–17.
- VAN DYKE, M. 1988 *An Album of Fluid Motion*. Stanford: The Parabolic Press.
- VILLERMAUX, E. & CLANET, C. 2002 The life of a flapping liquid sheet. *J. Fluid Mech.* **462**, 341–363.
- WEBER, C. 1931 Zum zerfall eines flüssigkeitsstrahles. *Z. Angew. Math. Mech.* **11**, 136–154.